*Proceedings of the Thirty-sixth (2026) International Ocean and Polar Engineering Conference*
*Orlando, Florida, USA, May 31-June 5, 2026*

*ISBN 978-1-880653-72-2; ISSN 1098-6189*

**www.isope.org**

# Analysis of Compressibility Effects on Sound Sources and Acoustic Propagation in Low-Mach-Number Noise

*Jiajia Qin[1], Fuchang Zhou[2], Yuan Zhuang[1], Decheng Wan[1*]*

[1] Computational Marine Hydrodynamics Lab (CMHL), School of Ocean and Civil Engineering,
Shanghai Jiao Tong University, Shanghai, China
[2] Wuhan Second Ship Design and Research Institute, Wuhan, China
[*]Corresponding Author

## ABSTRACT

Hydrodynamic flows are generally regarded as incompressible, while aerodynamic flows can yield different results depending on whether compressibility is considered. A deeper investigation of compressibility effects can help build a bridge between compressible aerodynamic and incompressible hydrodynamic flows. Many studies have focused on the influence of compressibility on the time-averaged flow statistics. However, the detailed unsteady features, such as vortex dynamics and fluctuating pressure, play a crucial role in noise generation but remain insufficiently understood, especially regarding the role of compressibility. In this study, a circular cylinder is employed as the research object to investigate the influence of compressibility on flow-induced noise. Both compressible and incompressible solvers are used to simulate the flows, and the characteristics of the sound source and sound propagation were compared. The acoustic results are obtained using the Ffowcs Williams-Hawkings (FW-H) equation. The results reveal the similarities and differences in acoustic characteristics between compressible and incompressible flows and establish a basis for numerically linking compressible aerodynamic noise with incompressible hydrodynamic noise.

KEY WORDS: Compressibility effect; FW-H equation; flow-induced noise; sound source and acoustic propagation

## INTRODUCTION

Low-Mach-number hydrodynamic flows are commonly treated as incompressible due to their negligible density variations (Fan et al., 2024). In contrast, even under low-Mach-number conditions, compressibility may influence aerodynamic flows and the associated noise (Lysenko et al., 2014; Khalighi, 2010; Wang et al., 2025). Clarifying the role of compressibility is therefore essential for establishing a consistent physical and numerical connection between hydrodynamic noise and aerodynamic noise.

Previous studies have primarily focused on the influence of compressibility on time-averaged flow statistics. It has been reported that, for low-Mach-number flows, the mean lift, drag, and Strouhal number predicted by compressible and incompressible solvers are in close agreement (Lysenko et al., 2012; Lysenko et al., 2014; Rajani et al., 2016; Wang et al., 2025). Nevertheless, compressibility may still affect local and instantaneous flow features, such as vortex dynamics and near-field structures (Lysenko et al., 2014), which are directly related to sound generation.

Flow-induced noise is inherently governed by unsteady flow characteristics, particularly fluctuating pressure and vortex shedding (Zhang et al., 2016; Turner and Kim, 2020; Zhao et al. 2025). Compared with time-averaged quantities, the influence of compressibility on these unsteady features remains insufficiently understood, especially in the context of low-Mach-number flows.

The Ffowcs Williams–Hawkings (FW-H) equation is widely used for aeroacoustics prediction based on acoustic analogy (Suresh et al., 2022; Zhang et al., 2022; Turner and Kim, 2022). Although true acoustic propagation cannot be resolved within incompressible flow solvers, the FW-H formulation allows the reconstruction of acoustic radiation by treating the medium as compressible in the propagation model. Consequently, the difference between compressible and incompressible flow-induced noise primarily originates from the acoustic source terms rather than the propagation process.

For the canonical problem of flow past a stationary circular cylinder at low Mach numbers, the dominant acoustic radiation is associated with dipole sources related to wall-pressure fluctuations (Zhuo et al., 2024). While previous studies have directly compared far-field noise predictions obtained from compressible and incompressible simulations and reported only minor differences in spectral characteristics (Khalighi, 2010), a systematic investigation of the underlying dipole source mechanisms, particularly wall-pressure fluctuations, is still lacking.

In this study, the effects of compressibility on low-Mach-number flow-induced noise are investigated with an emphasis on dipole sound sources and acoustic radiation. Flow past a circular cylinder is simulated using the incompressible solver pimpleFoam and the compressible solver rhoPimpleFoam, and far-field noise is predicted using the FW-H equation. By comparing the mean flow, wall-pressure fluctuations, and acoustic fields, this work aims to clarify the role of compressibility in low-Mach-number noise generation and to provide a physical basis for numerically linking compressible aerodynamic noise with incompressible hydrodynamic noise.

## THEORY AND METHODOLOGY

### Compressible Governing Equations

In addition to considering density variations, the compressible Navier-Stokes equations also incorporate energy, with the expressions shown below.

$$\frac{\partial \mathbf{v}}{\partial t}+\frac{\partial \mathbf{f}_{\mathbf{c},j}}{\partial x_j}=\frac{\partial \mathbf{f}_{\mathbf{v},j}}{\partial x_j} \tag{1}$$

where $\mathbf{v}$, $\mathbf{f}_{\mathbf{c},j}$, $\mathbf{f}_{\mathbf{v},j}$ represent the solution vector, convective flux vector, and diffusive flux vector, respectively.

$$\mathbf{v}=\begin{pmatrix}\rho\\ \rho u_1\\ \rho u_2\\ \rho u_3\\ \rho E\end{pmatrix},\mathbf{f}_{\mathbf{c},j}=\begin{pmatrix}\rho u_j\\ \rho u_1u_j+p\delta_{1j}\\ \rho u_2u_j+p\delta_{2j}\\ \rho u_3u_j+p\delta_{3j}\\ \rho u_jH\end{pmatrix},\mathbf{f}_{\mathbf{v},j}=\begin{pmatrix}0\\ \tau_{1j}\\ \tau_{2j}\\ \tau_{3j}\\ \tau_{ij}u_i-q_j\end{pmatrix} \tag{2}$$

Where $\rho$ denotes the density, $p$ represents the pressure, and $u_j$ represents the components of the velocity vector. $E$ and $H$ denote the total energy and total enthalpy, respectively, related by the expression $H=E+p/\rho$. Finally, $\tau_{ij}$ represents the viscous stress tensor.

### Incompressible Governing equations

The incompressible Navier-Stokes equations neglect density variations, and the governing equations consist of the continuity equation and the momentum equations:

$$\nabla\cdot\mathbf{u}=0 \tag{3}$$

$$\frac{\partial \mathbf{u}}{\partial t}+\nabla\cdot(\mathbf{uu})-\nabla\cdot(\nu\nabla\mathbf{u})=-\nabla P \tag{4}$$

Where $\nu$ denotes the kinematic viscosity and $P$ represents the dynamic pressure. In the following discussion, the compressible case is abbreviated as CNS, while the incompressible case is abbreviated as INS.

### Aeroacoustics model

The acoustic analogy equation employs the FW-H equation, and the Farassat 1A formula is its commonly used integral form solution. The acoustic pressure is obtained by summing the thickness noise derived from the monopole term and the loading noise derived from the dipole term, as follows:

$$p'_T=\frac{1}{4\pi}\left(\int_{f=0}\left[\frac{\rho_\infty(\dot{U}_n+U_n)}{r(1-M_r)^2}\right]_{ret}dS+\int_{f=0}\left[\frac{\rho_\infty U_n\{r\dot{M}_r+c_\infty(M_r-M^2)\}}{r^2(1-M_r)^3}\right]_{ret}dS\right) \tag{5}$$

$$p'_L=\frac{1}{4\pi c_0}\int_{f=0}\left[\frac{\dot{L}_r}{r(1-M_r)^2}\right]_{ret}dS+\frac{1}{4\pi}\int_{f=0}\left[\frac{L_r-L_M}{r^2(1-M_r)^2}\right]_{ret}dS+\frac{1}{4\pi c_0}\int_{f=0}\left[\frac{L_r\{r\dot{M}_r+c_0(M_r-M^2)\}}{r^2(1-M_r)^3}\right]_{ret}dS \tag{6}$$

$f(x,t)=0$ defines the surface of the solid body. $r$ is the magnitude of the vector from the source point to the observer. $M$ is defined as $M=v/c_\infty$, where $v$ is the velocity of the surface and $c_\infty$ is the speed of sound. $M_r$ is the Mach number in the radiation direction. A dot over a variable denotes differentiation with respect to time. The subscript “ret” denotes the retarded time. $U_n$ and $L_i$ is defined as shown in Eqs. 7~8, where $\delta_{ij}$ is the Kronecker delta, $u_n$ represents local normal velocity of the flow and $v_n$ represents local normal velocity of the surface. $L_r$ is the component of $L_i$ in the radiation direction, $L_M$ represents a Mach-number-related correction term, which is obtained as the inner product of $L_i$ with the local Mach number vector $M_i$.

$$U_n=(1-\frac{\rho}{\rho_\infty})v_n+\frac{\rho u_n}{\rho_\infty} \tag{7}$$

$$L_i=(p\delta_{ij}n_j+\rho u_i(u_n-v_n)) \tag{8}$$

## RESULTS AND DISCUSSION

Two circular-cylinder flow cases at a Mach number of 0.2 are investigated. The laminar case at Re=150 allows a clear examination of differences in acoustic propagation between incompressible and compressible formulations using a large computational domain, while the subcritical case at Re=3900, characterized by pronounced turbulent fluctuations and extensive reference data, is more suitable for investigating flow-induced noise dominated by dipole sound sources.

### The laminar case at Re=150

The present case is a two-dimensional simulation of flow past a circular cylinder. The cylinder diameter is $D$=3.3×10$^{-5}$ m, and the free-stream velocity is $U_\infty$=68 m/s. A circular computational domain is employed. In order to clearly examine acoustic propagation in compressible flow, the domain size is deliberately chosen to be sufficiently large, with a radius of $r$=100$D$, as illustrated in Fig. 1.

An O-type structured mesh with good orthogonality is adopted. The height of the first grid layer is set to $h_c/D$=8×10$^{-3}$, resulting in a wall-normal resolution of $y^+$=0.777, which satisfies the requirement of $y^+$<1. The wall-unit $y^+$ was evaluated as

$$y^+=\frac{u_\tau y}{\nu} \tag{9}$$

where $y$ is the distance from the wall to the first off-wall cell, $\nu$ is the kinematic viscosity, and $u_\tau$ is the friction velocity defined as

$$u_\tau=\sqrt{\frac{\tau_w}{\rho}} \tag{10}$$

with $\tau_w$ being the wall shear stress and $\rho$ the fluid density.
A total of 300 grids are distributed in both the circumferential and radial directions, yielding approximately 90,000 cells in the computational domain. The time step size is set to 1×10$^{-9}$ s, ensuring that the Courant number is maintained at approximately 0.25 to preserve numerical stability. The simulation is conducted for 150 vortex-shedding cycles, among which data corresponding to 75 cycles are sampled for post-processing. Owing to the low Reynolds number, the flow is computed using a laminar model.

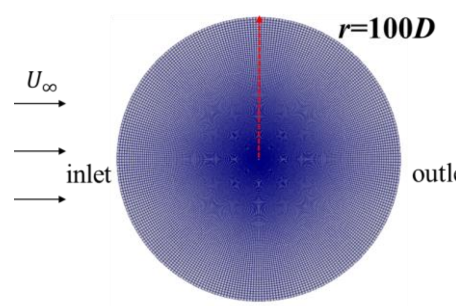


Fig. 1 Computational domain for the laminar case

Considering that both the Mach number and Reynolds number are relatively low and that the computational domain is sufficiently large, no sponge is applied in the compressible simulation. For CNS, the temperature is set to 293 K and the ratio of specific heats is specified as $\gamma$=1.4. A pressure outlet boundary condition of the waveTransmissive type is employed to minimize acoustic reflections at the far-field boundary. The dynamic viscosity is set to 1.78×10$^{-5}$ Pa·s, and the far-field density is specified as 1.19 kg/m$^3$. The flow is solved using the rhoPimpleFoam solver. To achieve a balance between numerical accuracy and stability, a second-order backward scheme is used for temporal discretization, the gradient terms are discretized using the Gauss linear scheme, and the divergence terms are treated with the linearUpwind scheme to suppress numerical oscillations (Lysenko et al., 2014).

For the incompressible case, the kinematic viscosity is set to $1.5\times10^{-5}$ m$^2$/s. The same second-order backward scheme is adopted for time discretization, while both gradient and divergence terms are discretized using the Gauss linear scheme. Both Gauss linear and Gauss linearUpwind are second-order schemes, exhibiting minimal differences in terms of spatial accuracy.

Table 1 presents a comparison of several statistics for the test cases, including the mean drag coefficient, maximum drag and lift amplitudes, and the Strouhal number. Fig. 2 displays the time-history curves of drag coefficient and lift coefficient. Specifically:

$$\Delta C_d = (C_{d,max} - C_{d,min})/2 \quad (11)$$

$$\Delta C_l = (C_{l,max} - C_{l,min})/2 \quad (12)$$

$$St = fD/U_\infty \quad (13)$$

Where $f$ represents the vortex-shedding frequency, which is obtained by the Fourier transform of the lift force.

Table 1. Fluid-dynamic statistics of the laminar case

| Case | $\overline{C_d}$ | $\Delta C_d$ | $\Delta C_l$ | $St$ |
|---|---|---|---|---|
| Inoue and Hakateyama (DNS) | 1.32 | 0.026 | 0.52 | 0.183 |
| Muller (DNS) | 1.34 | 0.026 | 0.52 | 0.183 |
| INS | 1.30 | 0.024 | 0.49 | 0.181 |
| CNS | 1.34 | 0.026 | 0.53 | 0.181 |

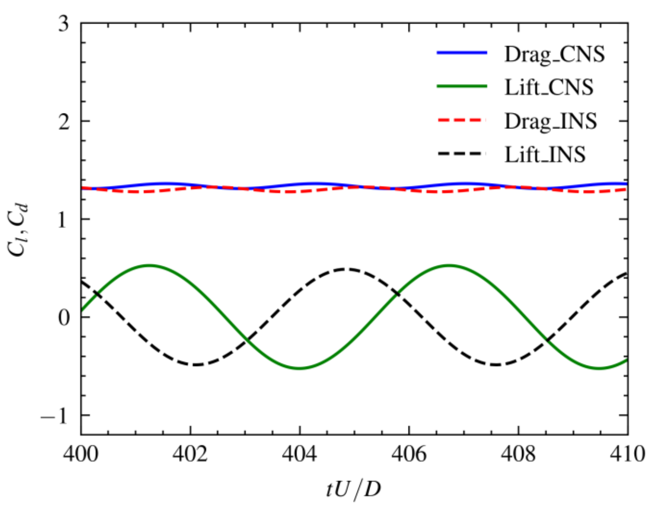


Fig.2 Time-history curves of drag coefficient and lift coefficient

As shown in the Table 1, the various statistics calculated by CNS are in good overall agreement with the reference results (Inoue and Hatakeyama, 2002; Müller, 2008), with relative errors generally maintained within 1%–2%. In comparison, the time-averaged statistics predicted by INS also maintain good consistency with the CNS and reference values. However, for unsteady quantities such as the maximum amplitudes of lift and drag, the accuracy of INS is significantly lower than that of CNS. These results indicate that under low Mach number conditions, compressibility has a limited impact on the time-averaged statistical characteristics of the flow field, but plays a crucial role in capturing its unsteady features.

To further analyze the influence of compressibility on the acoustic source terms themselves, the following discussion focuses on the wall pressure fluctuations, which are the primary source of dipole noise.

For this test case, the flow-induced noise is dominated by dipole sources, the intensity of which is primarily determined by the wall pressure fluctuations. Fig. 3 compares the root-mean-square (RMS) contours of the wall pressure fluctuations calculated by INS and CNS. Fig. 4 presents the distribution curves of the RMS wall pressure fluctuations along the cylinder surface at $z$=0, where the pressure fluctuations are non-dimensionalized using the far-field density and free-stream velocity. It can be observed that the wall pressure fluctuation contours exhibit good symmetry relative to the stagnation point. Compared to INS, the high-fluctuation regions predicted by CNS are more concentrated toward the upstream, with a slightly reduced coverage area. Meanwhile, the distribution area of the low-fluctuation regions is also diminished, leaving the majority of the wall surface at a moderate level of pressure fluctuation. From a quantitative perspective, the CNS results almost perfectly overlap with the INS predictions at the stagnation point and in the downstream regions, while the fluctuation amplitudes are slightly higher than those of INS in other areas. This trend is consistent with the previously discussed differences in the maximum amplitudes of lift and drag, where a lower level of wall pressure fluctuation corresponds to a smaller force coefficient amplitude.

Overall, INS and CNS show good agreement in terms of both the spatial distribution patterns and amplitude levels of the wall pressure fluctuations. This indicates that at low Mach numbers, the impact of compressibility on the dipole source terms, which are dominated by wall pressure fluctuations, is also relatively limited.

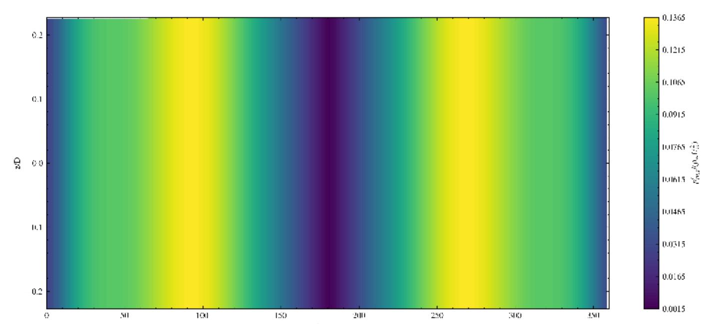

(a) CNS

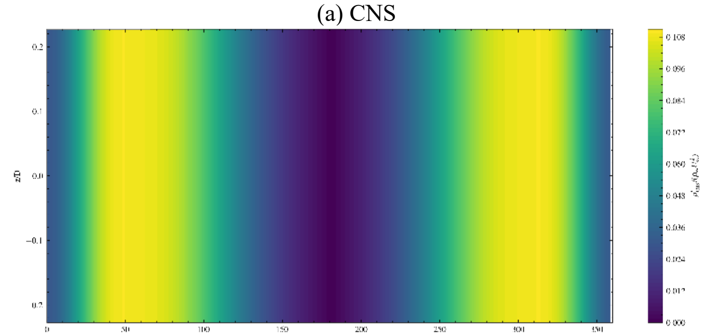

(b) INS

Fig. 3 The root-mean-square (RMS) wall pressure fluctuation contours

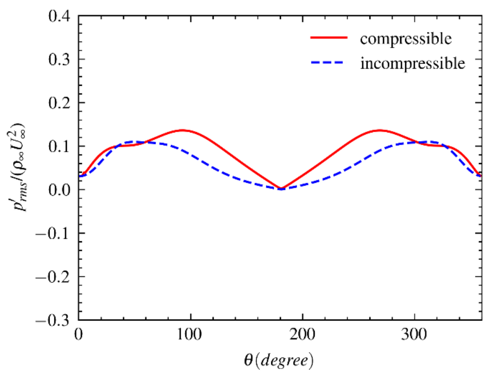


Fig. 4 The distribution curves of the RMS wall pressure fluctuations along the cylinder surface at $z$=0

Fig. 5 presents the instantaneous contours of pressure fluctuations throughout the entire flow field non-dimensionalized by the far-field density and sound speed, where a significant difference in acoustic propagation characteristics between CNS and INS can be clearly observed. Both methods are capable of capturing the alternating positive and negative pressure fluctuation structures on the upper and lower surfaces of the cylinder. However, in CNS, because the influence of density perturbations is explicitly considered, the pressure fluctuations radiate outward in a typical dipole pattern, allowing for a more realistic description of the physical process by which sound waves propagate with density disturbances. In contrast, since INS neglects density variations, its pressure perturbations propagate instantaneously in the calculation, making it difficult to directly reflect the finite propagation speed and spatial radiation characteristics of sound waves.

It should be noted that the FW-H equation models the acoustic propagation process via a wave equation form, which to some extent compensates for the inability to directly represent sound propagation in incompressible flow cases (Cianferra et al., 2019). Fig. 6 shows the root-mean-square (RMS) sound pressure distribution at 36 observers located at $r$=75$D$, where the circumferential coordinates correspond to different observation angles. It can be seen that the RMS sound pressure values predicted by INS are generally slightly lower than those of CNS, which is consistent with the conclusion that its wall pressure fluctuation amplitudes are smaller. However, in terms of overall trends, the acoustic directivity distributions obtained by the two methods are quite similar, and the difference in amplitude is limited. This suggests that for this low-Mach-number case, since the dipole source terms are largely consistent between the two computational methods, the overall impact of compressibility on the far-field flow-induced noise predictions remains minor.

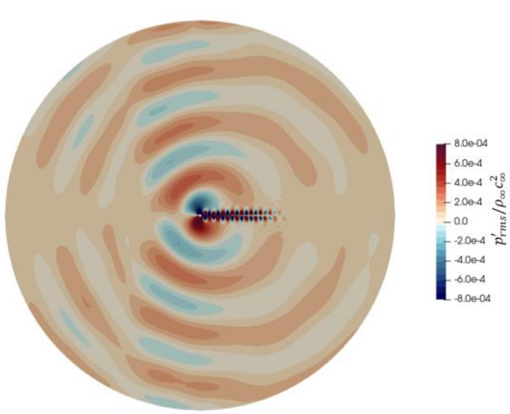


(a) CNS

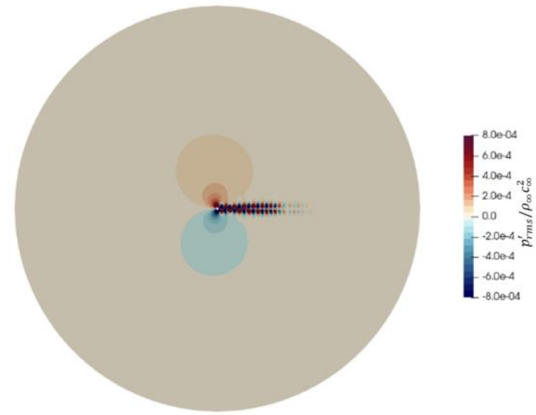


(b) INS

Fig. 5 The instantaneous contours of pressure fluctuations

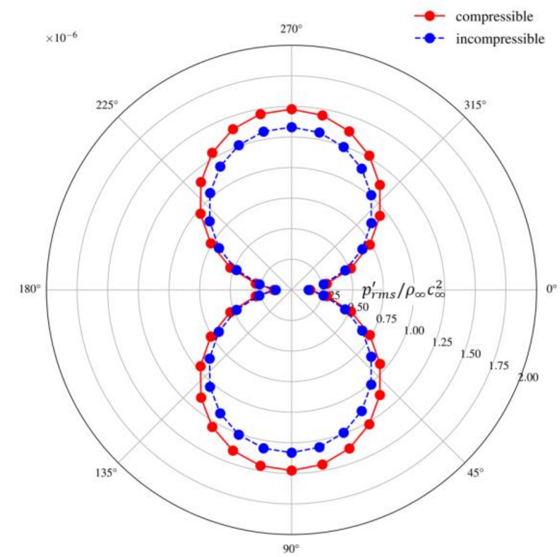


Fig. 6 The root-mean-square (RMS) sound pressure distribution at $r$=75$D$

## The subcritical case at Re=3900

In the aforementioned low-Reynolds-number 2D case, the flow is dominated by a regular 2D Karman vortex street, where the effects of compressibility on both acoustic sources and propagation are relatively limited. However, as the Reynolds number increases to Re = 3900, significant 3D instability structures and turbulent features emerge in the cylinder wake, making the 2D assumption inadequate for accurately describing the flow and its acoustic behavior (Chen et al., 2023). Consequently, this section employs 3D numerical simulations at Re = 3900 to further compare the predictive capabilities of the incompressible and compressible methods.

In this case, the cylinder diameter is $D$ = 0.00086 m and the free-stream velocity is $U_\infty$=68 m/s. The computational domain is defined as -15 < $x/D$ < 45, -15 < $y/D$ < 15, and $-\pi/2 < z/D < \pi/2$. An O–H type structured mesh is employed, as shown in Fig. 7. An O-grid is arranged within the region $r$=7.5$D$ around the cylinder to ensure near-wall resolution and orthogonality, with 300 grid points in both the circumferential and radial directions. The first-layer grid height is set to $h_c/D$=5×10$^{-4}$, corresponding to $y^+$=1, which satisfies the requirements for wall-resolved large eddy simulation (LES). The mesh naturally transitions to an H-grid in the outer regions, bringing the total grid count to approximately 3.25 million.

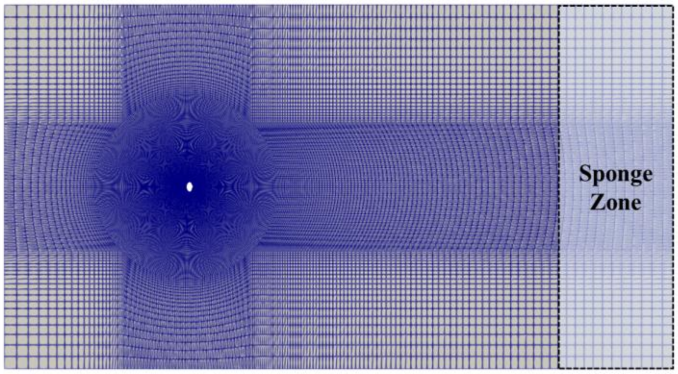


Fig. 7 Computational domain for the subcritical case

Wall-resolved LES is adopted for the numerical simulations. For the CNS case, the time step is set to $1\times10^{-8}$ s, and the Courant number is maintained at approximately 0.3 to balance numerical stability and temporal resolution. The simulation covers 200 vortex shedding cycles, with the latter 120 cycles used for statistical analysis. Given the higher Reynolds number and relatively limited domain, sponge zone is implemented at the domain boundaries to absorb outgoing disturbances and minimize boundary reflections. Other state parameters, boundary conditions, and discretization schemes remain consistent with the previous laminar case.

In contrast, the INS case exhibits more relaxed stability constraints. Thus, the time step is increased to $2\times10^{-8}$ s with a Courant number of approximately 0.5. The calculation also covers 200 cycles, with the final 120 cycles used for statistics. A second-order backward scheme is used for temporal discretization, while the Gauss linear scheme is applied to the gradient terms. The linearUpwind scheme is used for the divergence terms to suppress potential numerical oscillations under high-Reynolds-number conditions.

Table 2 presents the comparison of the main statistics. Fig. 8 displays the time-history curves of drag coefficient and lift coefficient and Fig. 9 displays the distribution of the time-averaged wall pressure. Figs. 10-14 present the profiles of mean velocity and mean Reynolds stress in the wake. The under-prediction of the Reynolds stresses can be attributed to a combination of modeling and numerical factors. First, the present simulations employ a wall-resolved LES with the WALE subgrid-scale model. Although the WALE model provides improved near-wall behavior, a small fraction of the turbulent fluctuations is still modeled rather than fully resolved, which can lead to a slight attenuation of the predicted Reynolds stress levels. Second, the Reynolds stresses are known to be sensitive to grid resolution and spatial filtering in LES. Despite the good agreement observed for the mean flow quantities and dominant flow features, some loss of small-scale turbulent energy may occur, resulting in lower predicted Reynolds stress magnitudes. Nevertheless, the overall spatial distributions and trends of the Reynolds stresses are well captured, and the level of under-prediction does not affect the main conclusions of the present study. It can be observed that within the wake, the mean velocity and Reynolds stresses predicted by INS are generally slightly lower than those of CNS. This discrepancy is more pronounced at $x/D$=1.54, reflecting a certain difference in the predictive performance of the two computational frameworks during the wake development. Nevertheless, INS and CNS maintain consistent profile shapes and trends, and both show good agreement with the experimental results (Parnaudeau et al., 2008).

Fig. 15 shows the instantaneous three-dimensional vortical structures of the flow past the cylinder, visualized using the Q-criterion with $Q = 30000$, as obtained from INS and CNS. Both solvers capture similar large-scale vortical structures in the wake region, indicating consistent predictions of the dominant flow features. Minor differences are mainly observed in the fine-scale vortical structures, which can be attributed to compressibility effects and differences in numerical treatment between the two solvers. Overall, the comparison demonstrates that the incompressible and compressible solvers provide comparable representations of the three-dimensional wake dynamics at this Reynolds number.

Table 2. Fluid-dynamic statistics of the subcritical case

| | $\overline{C_d}$ | $-C_p$ | $St$ |
|---|---|---|---|
| CNS | 0.94 | 0.84 | 0.208 |
| INS | 0.96 | 0.84 | 0.21 |
| Experiment | 0.99 | 0.9 | 0.208 |

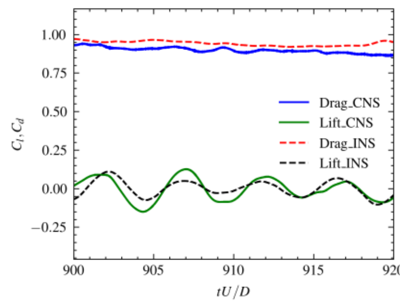


Fig. 8 Time-history curves of drag coefficient and lift coefficient

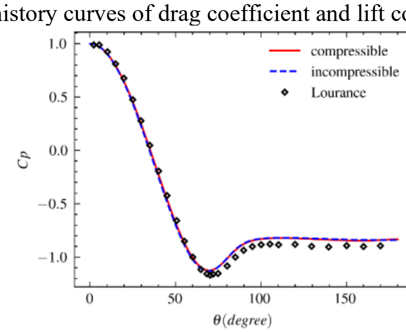


Fig. 9 The distribution of the time-averaged wall pressure

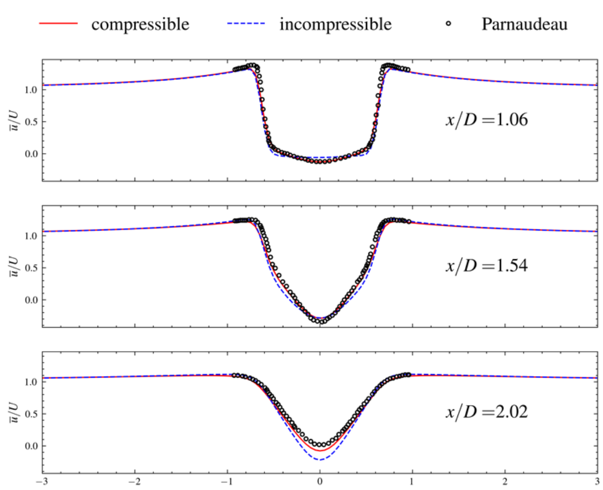


Fig. 10 Mean streamwise velocity profiles at $x/D$ = 1.06, 1.54, and 2.02

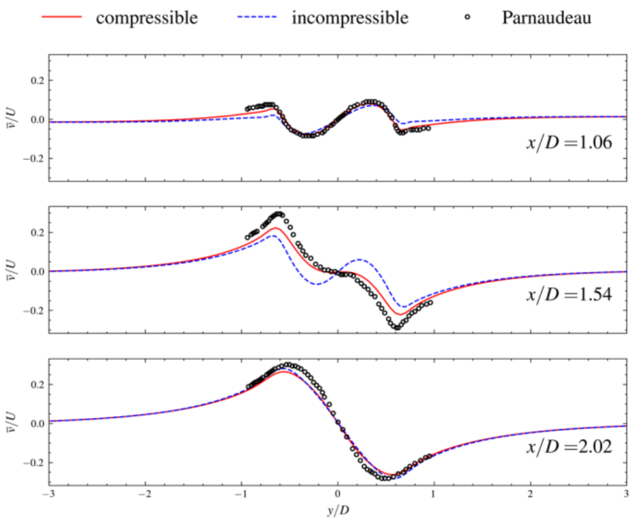

Fig. 11 Mean transverse velocity profiles at *x/D* = 1.06, 1.54, and 2.02

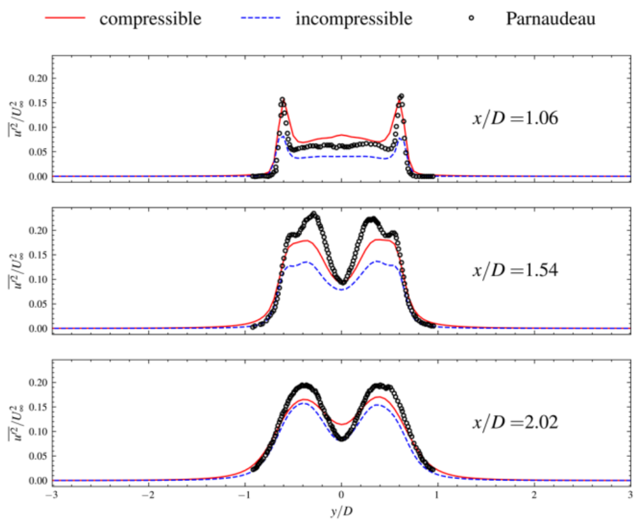

Fig. 12 Mean resolved Reynolds stress $\overline{u'u'}$ at *x/D* = 1.06, 1.54, and 2.02

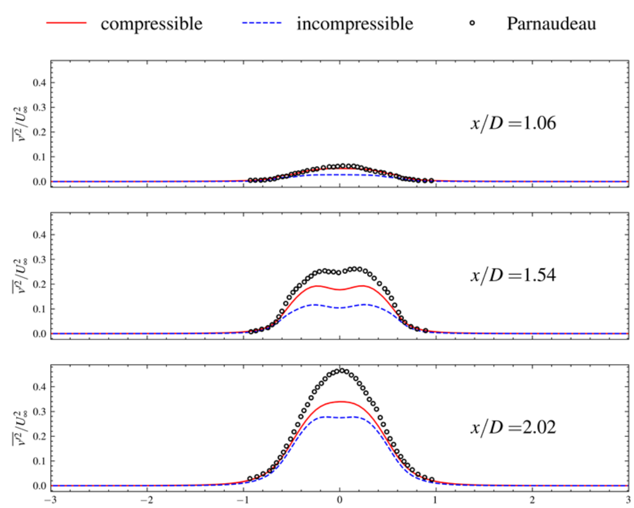

Fig. 13 Mean resolved Reynolds stress $\overline{v'v'}$ at *x/D* = 1.06, 1.54, and 2.02

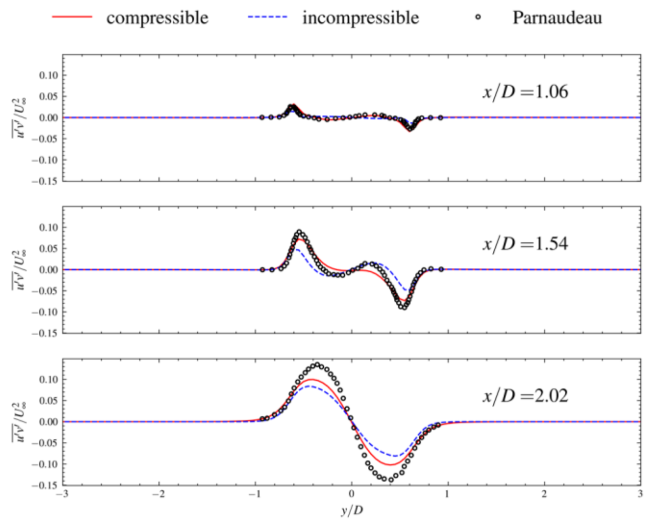

Fig. 14 Mean resolved Reynolds stress $\overline{u'v'}$ at *x/D* = 1.06, 1.54, and 2.02

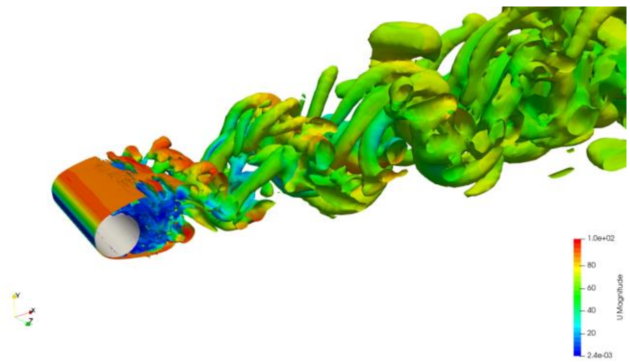
(a) CNS

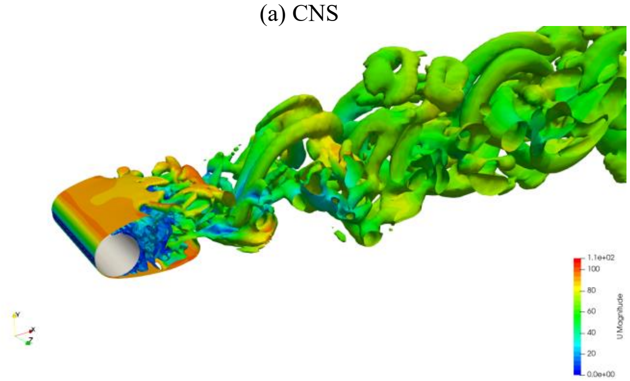
(b) INS

Fig. 15 Instantaneous three-dimension vortical structures of the flow past the cylinder: Q=30000.

Furthermore, Fig. 16 shows the noise prediction results at the observer (-1.26*D*, 1.5*D*). The sound pressure spectra obtained from both INS and CNS agree well with the reference DNS results, showing consistent overall trends. Where $\phi_{pp}$ represents the power spectrum density, and $p_{ref} = 2 \times 10^{-5} Pa$. Notably, the sound pressure amplitude of INS is slightly higher than that of CNS, which may be attributed to its slightly higher predicted mean drag coefficient and vortex shedding frequency, leading to a corresponding increase in dipole source intensity.

Fig. 17 presents the comparison of the pressure fluctuation spectra. It can be observed that at the near-field observers, the spectra predicted by INS and CNS are closely matched in terms of both dominant frequencies and amplitude levels, with minimal discrepancies. This indicates that at low Mach numbers, compressibility has a limited impact on the near-field unsteady pressure characteristics. However, in the far-field region, since the INS flow field itself does not account for authentic acoustic propagation mechanisms, its instantaneous pressure perturbations cannot propagate outward over time. This leads to a significant difference between the far-field pressure fluctuations extracted directly from the flow field and the CNS results.

Nevertheless, the FW-H equation effectively describes the sound wave propagation process by reconstructing the unsteady perturbations in the flow field as acoustic source terms in a wave equation form, thereby compensating for the deficiency of incompressible flow in modeling acoustic propagation. As shown in Fig.18, in the far-field noise spectra calculated via the FW-H equation, the results of INS and CNS exhibit good agreement in terms of overall spectral shape, dominant frequency, and amplitude levels. In fact, a total of 18 observers were arranged every 10° at a distance of 23.06$D$ from the coordinate origin. The noise spectra obtained from INS and CNS show negligible differences at these locations. For brevity, only the results at 30°, 90°, and 150° are presented here.

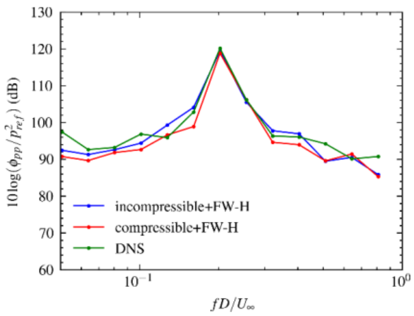


Fig. 16 Noise results of INS and CNS at (-1.26$D$, 1.5$D$)

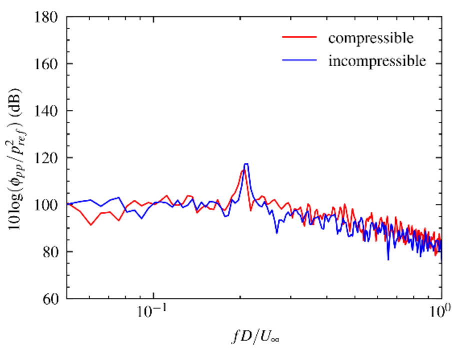


(a) near-field observer (2.35$D$, 2.28$D$)

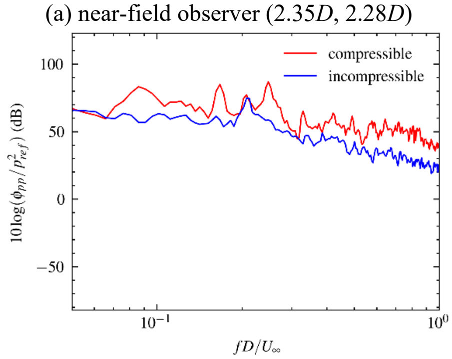


(b) far-field observer (-10$D$, 12$D$)

Fig. 17 Power spectrum of dynamic pressure

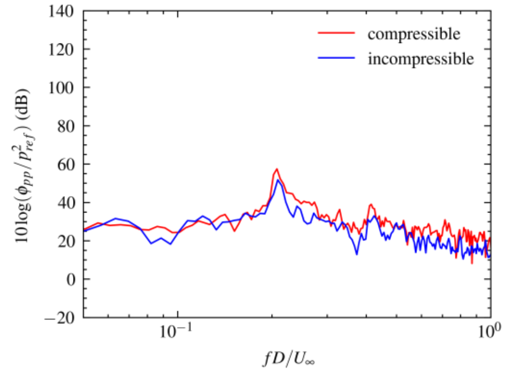


(a) observer (19.97$D$, 11.53$D$)

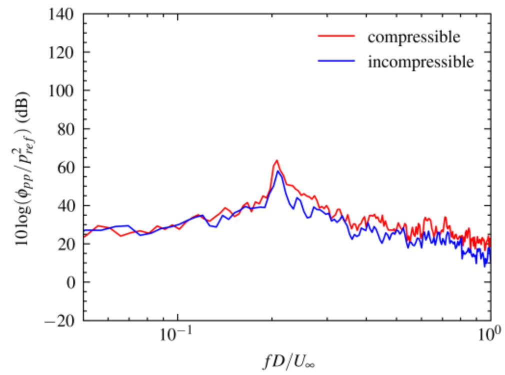


(b) observer (0, 23.06$D$)

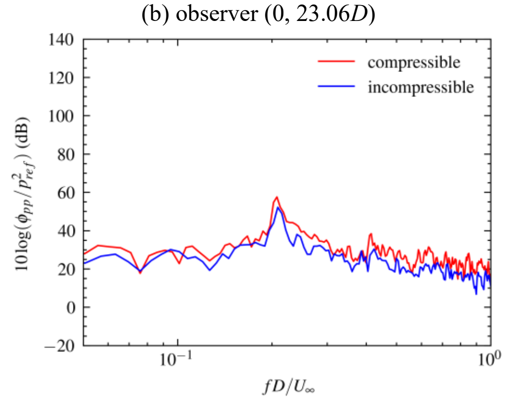


(c) observer (-19.97$D$, 11.53$D$)

Fig. 18 Power spectrum of far-field sound pressure

Consequently, it can be concluded that although the INS case cannot directly characterize the authentic far-field acoustic propagation at the flow-field level, its predictions for the time-averaged statistics and near-field pressure fluctuations are basically consistent with those of CNS. When combined with the FW-H equation, the incompressible case can also accurately reconstruct the propagation characteristics of sound waves, ultimately yielding far-field noise results similar to those of CNS. Compared with CNS, employing INS for flow-field solution not only avoids the numerical stability issues often encountered with compressible solvers under high-Reynolds-number conditions but also maintains consistency with incompressible hydroacoustic problems at the governing equation level. This makes the establishment of numerical correlations between aeroacoustics and hydroacoustics more physically consistent and reasonable.

## CONCLUSIONS

This study focuses on flow around a circular cylinder to systematically compare the performance of compressible (CNS) and incompressible (INS) solvers in terms of flow field prediction, acoustic propagation representation, and noise calculation under both laminar and subcritical regimes. The results indicate that INS and CNS yield generally consistent results with minimal discrepancies in terms of time-averaged flow statistics and key unsteady features, such as wall pressure fluctuations.

Since the incompressible framework does not inherently account for authentic acoustic propagation mechanisms, INS cannot directly characterize the process of pressure perturbations propagating to the far field at the flow-field level. Consequently, far-field pressure fluctuations extracted directly from INS exhibit significant deviations, making them unsuitable for noise prediction. However, by reconstructing the acoustic propagation process via the FW-H equation, the incompressible case can accurately describe the radiation characteristics of sound waves, ensuring that the far-field noise results predicted by INS remain in good agreement with those of CNS.

It should be noted that while INS and CNS are not entirely equivalent at the physical modeling level, such differences are typically within an acceptable range under low-Mach-number conditions. Based on these findings, for low-Mach-number flow-induced noise problems, it is highly reasonable to employ an incompressible solver for flow simulation in conjunction with the FW-H equation for acoustic analysis. On one hand, this approach avoids the numerical stability issues associated with compressible solvers at high Reynolds numbers. On the other hand, its governing equations are consistent with those used in incompressible hydroacoustic problems, facilitating the establishment of a unified numerical analysis framework with greater physical consistency between aeroacoustics and hydroacoustics.

## ACKNOWLEDGEMENTS

This work is supported by the National Natural Science Foundation of China (52571359, 52131102), to which the authors are most grateful.

## REFERENCES

Chen, G, Zang, B, and Azarpeyvand, M (2023). “Numerical investigation on aerodynamic noise of flow past a cylinder with different spanwise lengths,” *Physics of Fluids*, 35(3), 035128.

Cianferra, M, Ianniello, S, and Armenio, V (2019). “Assessment of methodologies for the solution of the Ffowcs Williams and Hawkings equation using LES of incompressible single-phase flow around a finite-size square cylinder,” *Journal of Sound and Vibration*, 453, 1-24.

Fan, G, Liu, Y, Zhao, W, et al. (2024). “Effect of wall stress models and subgrid-scale models for flow past a cylinder at Reynolds number 3900,” *Physics of Fluids*, 36(1), 015152.

Inoue, O, and Hatakeyama, N (2002). “Sound generation by a two-dimensional circular cylinder in a uniform flow,” *Journal of Fluid Mechanics*, 471, 285-314.

Khalighi, Y (2010). *Computational Aeroacoustics of Complex Flows at Low Mach Number*, Ph.D. Thesis, Stanford University.

Lysenko, D A, Ertesvåg, I S, and Rian, K E (2012). “Large-eddy simulation of the flow over a circular cylinder at Reynolds number 3900 using the OpenFOAM toolbox,” *Flow, Turbulence and Combustion*, 89(4), 491-518.

Lysenko, D A, Ertesvåg, I S, and Rian, K E (2014). “Large-eddy simulation of the flow over a circular cylinder at Reynolds number $2\times 10^4$,” *Flow, Turbulence and Combustion*, 92(3), 673-698.

Müller, B (2008). “High order numerical simulation of aeolian tones,” *Computers & Fluids*, 37(4), 450-462.

Parnaudeau, P, Carlier, J, Heitz, D, et al. (2008). “Experimental and numerical studies of the flow over a circular cylinder at Reynolds number 3900,” *Physics of Fluids*, 20(8), 085101.

Rajani, B N, Kandasamy, A, and Majumdar, S (2016). “LES of flow past circular cylinder at Re=3900,” *Journal of Applied Fluid Mechanics*, 9(3), 1421-1435.

Suresh, T, Szulc, O, and Flaszynski, P (2022). “Aeroacoustic analysis based on FW–H analogy to predict low-frequency in-plane harmonic noise of a helicopter rotor in hover,” *Archives of Mechanics*, 74(2-3).

Turner, J M, and Kim, J W (2020). “Aerofoil dipole noise due to flow separation and stall at a low Reynolds number,” *International Journal of Heat and Fluid Flow*, 86, 108715.

Turner, J M, and Kim, J W (2022). “Quadrupole noise generated from a low-speed aerofoil in near-and full-stall conditions,” *Journal of Fluid Mechanics*, 936, A34.

Wang, Q, Shao, M, Duan, L, et al. (2025). “Effect of compressibility on flow-induced noise predictions at low Mach numbers,” *Physics of Fluids*, 37(12), 126128.

Zhang, N, Hua, X, and Xing, W (2016). “Computation of vortical flow and flow induced noise by large eddy simulation with FW-H acoustic analogy and Powell vortex sound theory,” *Journal of Hydrodynamics, Ser. B*, 28(2), 255-266.

Zhang, Y, Xiao, Y, Liu, R, et al. (2022). “Aeroacoustic prediction based on large-eddy simulation and the Ffowcs Williams–Hawkings equation,” *Advances in Aerodynamics*, 4(1), 19.

Zhao, Y H, Ding, J, Weng, P F, et al. (2025). “Method of aerodynamic noise source identification for cylinder flows,” *Journal of Fluid Mechanics*, 1012, A13.

Zhuo, Y, Qin, G, and Ye, X (2024). “Fluid-acoustic monolithic simulation based on spectral element method to solve flows past a slotted circular cylinder at low Reynolds numbers,” *AIP Advances*, 14(9), 095113.